

Research Article

Simulation Study of Breakage in Coral Sand Particles under Dynamic Confined Compression

Jianping Wang,^{1,2} Haotian Zhang ,¹ Tao Chen ,¹ and Linjian Ma ¹

¹Defense Engineering College, Army Engineering University of PLA, Nanjing 210007, China

²Navy Institute of Engineering Design and Research, Beijing 100070, China

Correspondence should be addressed to Haotian Zhang; 335733770@qq.com and Tao Chen; 857704494@qq.com

Received 15 September 2022; Revised 13 January 2023; Accepted 10 February 2023; Published 8 March 2023

Academic Editor: Annalisa Greco

Copyright © 2023 Jianping Wang et al. This is an open access article distributed under the Creative Commons Attribution License, which permits unrestricted use, distribution, and reproduction in any medium, provided the original work is properly cited.

This paper reports a simulation-based dynamic confined compression analysis of coral sand under an impact load using the discrete element method (DEM). The evolution of particle breakage on the mesoscale was studied by investigating force chain distributions, crack development, and breakage modes. Crushable sand particles were simulated by replacing rigid particles with flexible basic unit aggregates. The Weibull parameters were incorporated within the mesoscopic parameters of particles, and random numbers were introduced. The obtained results for particle strengths were consistent with the experimental data. The numerical results demonstrated that the force chain was significantly strengthened along the loading axis during loading and weakened during unloading. The cracks were primarily generated along the strong force chain, and particle breakage caused the strong force chain to move towards relatively more complete fragments nearby. The crack was primarily oriented along the loading axis, and its anisotropy was observed to decrease with an increase in the load. Before yielding, particle breakage in the specimen was dominated by attrition at the edges and corners. After yielding, the crack extended into the particle perpendicular to the intergranular contact surface and was deflected by the simultaneous influence of pores. The fracture and shattering of particles occurred successively, and the consequent fall-off and slip filling of the fragments promoted the deformation development.

1. Introduction

Coral sand is primarily distributed in coastal areas between 30°N and 30°S. It is a special rock-soil medium formed from the remains of marine organisms under long-term geological processes. In recent decades, this precious marine resource has been widely used in island and reef engineering constructions. On the one hand, coral sand can be used as the aggregate of coral concrete during the construction of conventional coastal buildings [1, 2]. On the other hand, loose coral sand media can be incorporated within layered structures in protection engineering. Coral sand particles exhibit the characteristics of high angularity, high porosity, and irregular shapes, which are different from those of terrestrial sand such as quartz sand. Scholars have carried out extensive experimental studies on the characteristics of coral sand particles. Ma et al. [3] studied the quasi-static mechanical properties of individual coral sand particles and

found that the particle crushing strength conforms to the Weibull statistical law. The characteristic strength decreases with an increase in the particle size and increases with an increase in the loading rate. Bryant et al. [4] and Coop [5] conducted confined compression tests on coral sand and found that the increase of carbonate content increases the compression index and reduces the compression rebound degree. Wang et al. [6] found that the relationship between the relative breakage index of nonuniform coral sand and the vertical stress could be expressed by a power function, and this relationship is related to the initial relative density. Further, it has also been established that nonuniform coral sand exhibits higher deformation resistance than uniform coral sand. Datta et al. [7] performed a triaxial test on coral sand and concluded that an increase in confining pressure accelerates the development of particle breakage. Luzzani and Coop [8] found that the volumetric strain of coral sand does not attain stability even when the shear strain reaches

60%. Thus, they suggested prioritizing the strain index during the definition of the strength of coral sand in engineering practice. Based on experimental observations, Wang et al. [9] proposed a path-dependent model of incremental particle breakage evolution, which reasonably considered the effects of breakage history and the current state of stress on the breakage rate. In protection engineering, coral sand is often used to reduce and disperse explosive loads. Therefore, accurate determination of the attenuation of stress waves in coral sand is greatly beneficial to associated engineering design and construction. In this regard, existing studies have primarily resorted to the Split Hopkinson Pressure Bar (SHPB) test [10, 11]. Yu et al. [12] compared the attenuation effects of impact stress waves in coral sand and quartz sand, and concluded that the former exhibits a better stress wave attenuation effect than the latter. Moreover, the attenuation effect was observed to be independent of wave amplitude but inversely proportional to wavelength and relative density.

Although the macromechanical response of granular materials has been well explored, relatively few descriptions of meso-mechanisms have been attempted due to the limitations of the aforementioned laboratory tests. With recent developments in computing technology, it has become possible to utilize numerical simulations to investigate the force chain network of granular materials and the development of internal cracks. Hence, it is possible to analyse the particle breakage processes, results, and mechanisms on the mesoscale. McDowell and Harireche [13] applied a DEM-based approach to the study of sand breakage. They utilized bonding bonds to aggregate the basic units into particles, and considered the fracture of bonding bonds to indicate the breakage of particles. Elghezal et al. [14] conducted a laboratory particle compression test and performed corresponding DEM simulations. A comparison between the experimental and simulated results revealed good agreement between the two, indicating the viability of DEM as an effective tool to predict breakage behaviours of granular materials. Kuang et al. [15] studied the effects of size and coordination number (CN) on particle breakage. They found that the tensile strengths of particles decrease with an increase in size and increase with an increase in the CN. Further, an increase in the CN was observed to transform the failure mode of particles from brittle failure to ductile failure. Zhao et al. [16] simulated the breakage behaviours of irregular particles and found that the larger the maximum curvature near the loading contact point, the lower the particle strength. Liu and Lok [17] analysed the effect of void ratio on one-dimensional (1D) compression of particles. They found the normalized octahedral shear stress subjected by the loose specimen to be more dispersed, inducing earlier particle breakage and lower yield stress. Zhang et al. [18] used DEM to generate crushable aggregates, performed true triaxial numerical tests, and studied the influence of initial confining pressure and intermediate principal stress on soil macroresponse and particle breakage. Huang et al. [19] defined equivalent volume diameter and average CN and studied variations in the particle gradation and CN of sand during dynamic confined compression. They argued that the

compression deformation of the material is mainly caused by particle breakage after yielding. Yang et al. [20] analysed the development of the meso-structure of sand during the direct shear test and noted that the anisotropy of the contact force increases significantly during the test and then tends to stabilize after the peak.

As summarized above, a large number of laboratory tests and several numerical simulations of soil particle breakage have been carried out to investigate the breakage of coral sand particles. These studies have focused on the influences of factors such as size, density, and shape on the responses of materials such as strength and failure modes, which are of great significance to engineering. However, few studies have investigated the evolution of particle breakage, and research on the breakage behaviours of particles under impact load is even rarer. Given that empirical laboratory research on the dynamic mechanical properties of coral sand is based on the SHPB device, the utilization of numerical methods to simulate and analyse pertinent breakage behaviours of coral sand particles is the primary premise to connect the macroscopic and mesoscopic characteristics of sand particles under dynamic loading conditions. It is helpful to deepen the understanding of the constitutive relationship of sand. Therefore, in this paper, we employed DEM to conduct the dynamic confined compression test on sand specimens and analysed the development and evolution of meso-cracks, force chain distributions, and breakage modes. The simulation method is suitable for further parameter analysis on the dynamic mechanical properties of coral sand, which can provide validation and supplement for laboratory tests and theoretical models. The feasible procedure of forming breakable particles can be utilized in explosion prototype tests or real case studies. The results of this paper are expected to provide beneficial references for island and reef engineering and construction.

2. Simulation Method for the Dynamic Confined Compression Test of Coral Sand

In this paper, DEM-based PFC^{2D} (Particle Flow Code of two-dimensional) has been used to establish the numerical model for the dynamic confined compression of coral sand. The SHPB test system and the specimen model are illustrated in Figure 1. Both the incident bar and the transmission bar were taken to have lengths of 2000 mm, diameters of 35 mm, densities of 2700 kg/m³, and elastic moduli of 70 GPa. The basic elements constituting the pressure bars were arranged regularly at equal diameters. At the loading end, large-diameter elements were transitioned into small-diameter elements to ensure calculation efficiency and improve the measurement accuracy [21]. A semiempirical method was adopted to determine the meso-parameters of the pressure bars; i.e., some parameters (such as size, density, and modulus) were calculated based on real macroparameters, while the values of others were derived from other available studies [22]. The parameter values are listed in Table 1. During the numerical simulation, a velocity pulse was

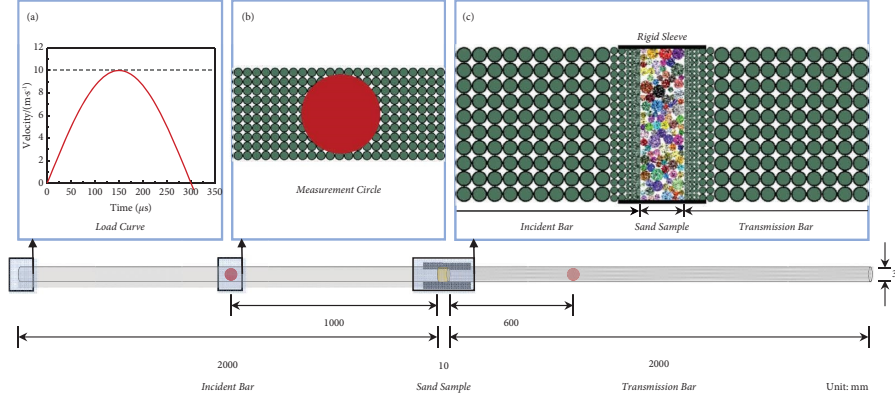


FIGURE 1: Numerical model of the SHPB device.

applied at the loading end of the incident bar, and the stress wave propagating through the pressure bar was measured using the measuring circle, as depicted in Figures 1(a) and 1(b), respectively.

Before generating the specimen, a rectangle position was reserved between the pressure bars, and nondeformable rigid walls were set up on the upper and lower sides to simulate the rigid sleeve in the laboratory test, as depicted in Figure 1(c). The coral sand specimens were prepared in the rectangular area enclosed by the pressure bar and the rigid walls, and the basic process is illustrated in Figure 2. Initially, rigid particles with a certain gradation (see Figure 3) were generated, as shown in Figure 2(a). Subsequently, the contact conditions between particles were set and iterated over 1000 time-steps. The particle position was calculated and updated based on the force-displacement law and Newton's second law, as shown in Figure 2(b). Then, the particles were replaced by smaller basic unit aggregates, as shown in Figure 2(c). The specific algorithm is as follows: The previous rigid particles are placed in the layer I. Another layer, i.e., the layer II, was created within the same rectangular area and filled with close-set fine basic units. In layer II, the basic units covered by the rigid particles in layer I are retained and saved as an aggregate. Remaining particles as well as the layer I are deleted. Finally, bonding bonds were added between basic units that belonged to the same aggregate, as shown in Figure 2(d). All particles until this step were crushable, bonding bonds between particles were set to be linear contacts, and the entire specimen was discrete. The aggregated specimen exhibited a diameter of 35 mm, a thickness of 10 mm, and it comprised an aggregate of 107 crushable individual particles, containing 11317 basic units. In the initial state, the number of bonding bonds was 23787, and the number of linear contacts was 806.

The meso-parameter configurations of coral sand particles are presented in Table 1. Via the simulation pretests on single coral sand particles, the single particle crushing strength under impact load was observed to exhibit an approximately linear relationship with the mesoscopic strength parameters. Hence, the strength parameters of particles in one sand sample were referred to the single particle breakage laboratory test data conducted on a 6 mm

diameter SHPB [11], which were set as a Weibull distribution:

$$\begin{cases} \text{Pb_ten} = \text{Pb_ten}_0 \cdot \exp\left(\frac{\ln(\ln(1/P_R))}{m_0}\right), \\ \text{Pb_coh} = \text{Pb_coh}_0 \cdot \exp\left(\frac{\ln(\ln(1/P_R))}{m_0}\right), \end{cases} \quad (1)$$

where Pb_ten_0 and Pb_coh_0 denote the benchmark tensile cohesion strength, respectively; i.e., when Pb_ten and Pb_coh are Pb_ten_0 and Pb_coh_0 , respectively, the macroscopic particle strength is σ_{f0} . m_0 denotes the Weibull modulus, and P_R denotes a random number uniformly distributed between 0 and 1. The aforementioned method was followed to simulate particle breakage. The survival curves of laboratory tests and numerical results are depicted in Figure 4. A characteristic strength of 9.67 MPa and a Weibull modulus of 2.41 were observed via the laboratory test, while a characteristic strength of 9.89 MPa and a Weibull modulus of 2.44 were obtained via the numerical test. A comparison between the two revealed good agreements.

3. Results and Discussion

3.1. Force Chain and Crack Evolution Law. In the numerical dynamic compression test on sand specimens, the mesoscale breakage of particles was manifested as the fracture of bonds between the basic units, i.e., the development of meso-cracks [23]. To facilitate the analysis of mesoscale breakage development, the ratio of the number of meso-cracks (i.e., the number of fractured bonding bonds) to the number of initial bonding bonds was used to characterize the breakage degree of sand, which was defined to be the mesoscopic breakage rate [24]. Figure 5 depicts the e - $\lg\sigma$ compression curve and the variation curve of the mesoscopic breakage rate with respect to stress. The four representative stages are indicated by arrows in Figure 5, as well as the yield point obtained by fitting.

From both the compression curve and the mesoscopic breakage rate variation curve, the void ratio was observed to decrease slowly with an increase in stress during the initial

TABLE 1: Numerical simulation of meso-parameters.

	Contact model	Density ($\text{kg}\cdot\text{m}^{-3}$)	Modulus (GPa)	Stiffness ratio	Tensile strength (MPa)	Cohesion strength (MPa)	Friction angle ($^{\circ}$)
SHPB	Parallel bond	2700	70	2.5	10^{100}	10^{100}	20
Particle	Parallel bond	1000	5.0	1.0	Pb_ten	Pb_coh	7.5

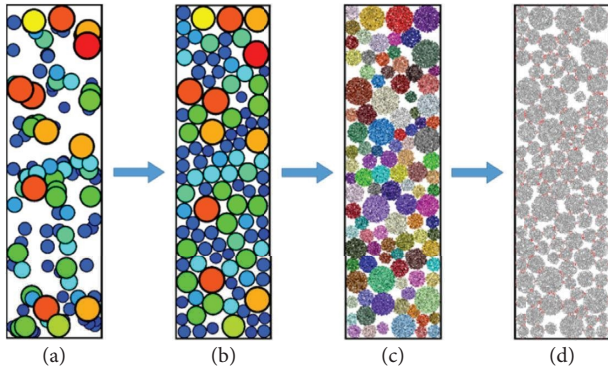


FIGURE 2: The basic preparation process of numerical specimens.

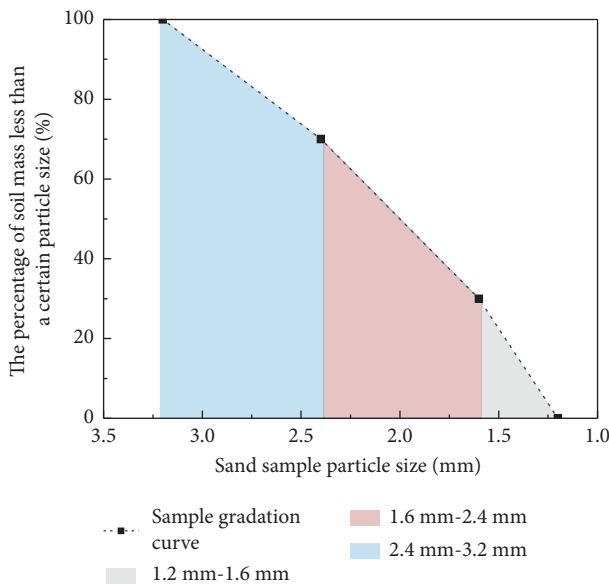


FIGURE 3: Sand specimen gradation.

phase of the loading stage. The specimen did not yield even when the axial stress reached stage A. The appearance and slow proliferation of meso-cracks indicated that particle breakage was not obvious. As the stress continued to increase, the material entered the yielding stage, in which particle breakage accelerated significantly. When the stress reached stage B, the breakage rate, which was observed to increase linearly with an increase in the axial stress, increased to a stable stage. During this stage, the rate of decrement of the void ratio accelerated significantly, indicating the aggravation of the compression deformation of the specimen by particle breakage in the postyielding phase [25]. Shi et al. [26] performed the laboratory high-stress 1D compression test on Toyoura sand using particle flow software and obtained similar results. During stage C, cracks increased at a stable and high rate, and obvious particle breakage was detected. Following stage D, the specimen entered the unloading stage, and the stress began to decrease, while the mesoscopic breakage rate of the specimen continued to increase.

From the perspective of the mechanics of particulate matter, the particle system is connected via internal contact, which gradually forms a path capable of transferring loads, that is, forming a force chain. The intricate force chains are intertwined to constitute a force chain network inside the particle system. Paths that bear greater stress and conduct higher numbers of external loads constitute strong force chains; weak force chains are correspondingly defined. The nature, strength, and distribution of stress between particles are reflected in the force chain network directly [27]. The distribution of force chains and meso-cracks corresponding to stages A, B, C, and D are depicted in Figure 6. In the force chain distribution diagram, blue represents pressure, green represents tension, the thickness of the force chain represents the magnitude of stress, and the short red lines denote the meso-cracks generated by the fracture of bonding bonds. The meso-crack development diagram depicts the distribution of cracks in the sand specimen.

By consulting Figure 5 as well, it is clear that the initial loading section corresponds to the portion between load application and stage A. In this section, the force chain formed by the contact force between particles inside the specimen was observed to be relatively weak, and the contact force was not strong enough to induce obvious particle breakage. However, uneven forces were present within the specimen, triggering local particle breakage, which resulted in a small number of cracks. Compared to the initial state, the void ratio of the specimen decreased slightly during stage A. This can be primarily attributed to particle slippage and partial compaction of external pores. When the load developed to stage B, the overall force chain was strengthened, the strong and weak force chains intersected each other, and the distribution became more uniform. At this stage, meso-cracks were generated along the strong force chain. Compared to that in stage B, the force chain network in stage C was further strengthened as a whole, the stress transmission path became clearer, and the strong force chain was oriented primarily along the loading axis. Simultaneously, part of the strong force chain broke and disappeared with the breakage of particles. The newly formed strong force chains were located on both sides of the site of breakage, and the load was borne by the more complete fragments after the disintegration of the force chain. Following stage D, the stress entered the unloading stage, and the force chain began to weaken.

Further, the development of anisotropy in the direction of meso-cracks was also analysed, as illustrated in Figure 7. The crack direction was primarily horizontal as the entire specimen was subjected to a horizontal impact load. When particles are primarily subjected to horizontal contact forces, tensile stress is generated in the vertical direction, leading to the breakage surface to be horizontally oriented. With an increase in the load, the degree of anisotropy along the crack direction was observed to decrease. This can be attributed to local stress deflection induced by the breakage, leading to an increase in the randomness of the fracture directions of bonding bonds and greater uniformization of the crack angle distribution [28].

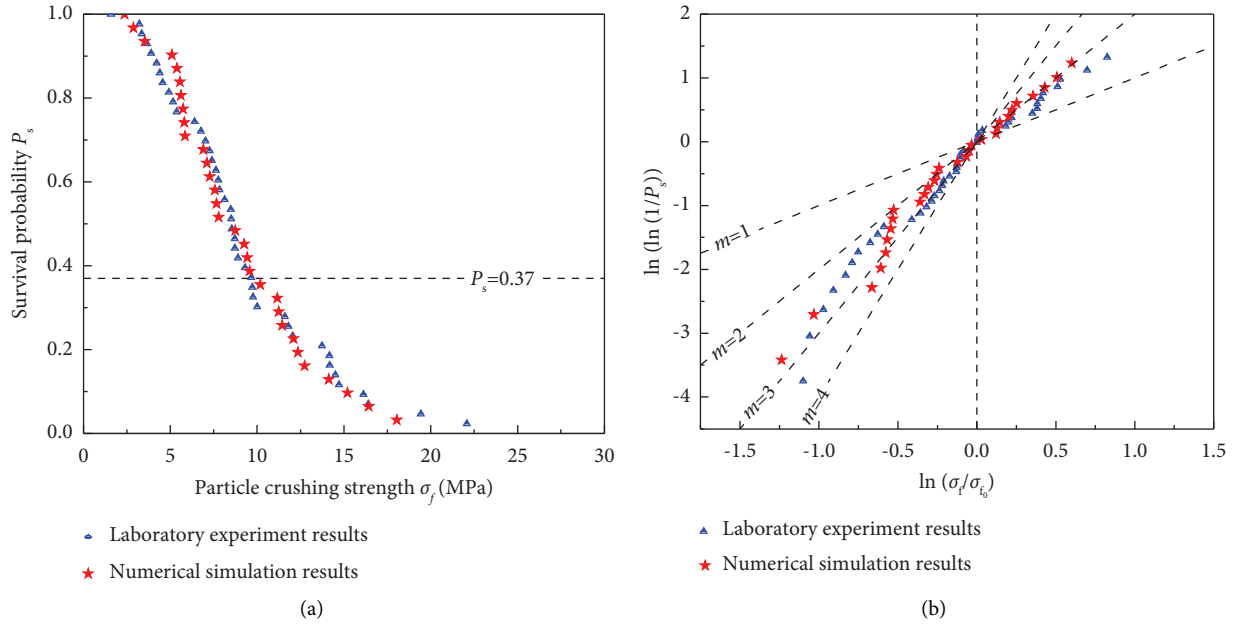


FIGURE 4: Comparison of the survival curves obtained via the numerical and laboratory particle breakage tests. (a) Survival probability curves, (b) normalized survival probability curves.

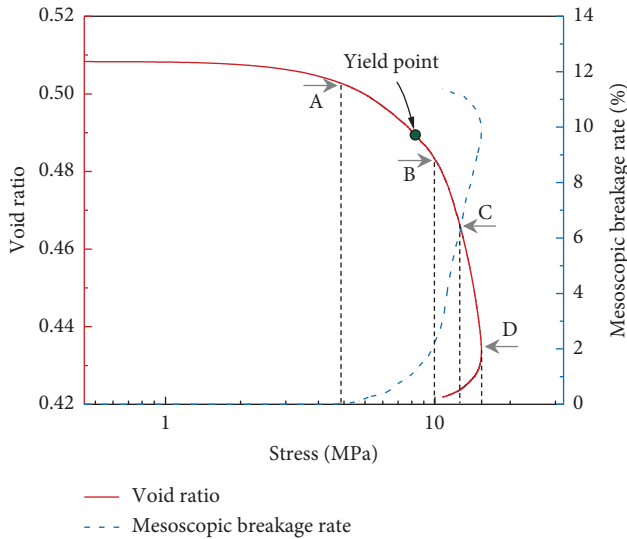


FIGURE 5: The e - $\lg\sigma$ compression curve and the mesoscopic breakage rate development curve during the numerical dynamic confined compression test on the sand specimen.

3.2. Evolutionary Law for Modes of Breakage. To address the demand for research on breakage mechanisms, breakage modes have been classified by many scholars. In particular, Guyon and Trodec [29] classified breakage modes into three categories: (I) Fracture, in which particles are broken into fragments of roughly equal size; (II) Attrition, in which the outer layers of particles break, generating a fragment of slightly smaller size than the original one and several dissociated small fragments; (III) Abrasion, in which the particle size remains almost unchanged and only fine particles are produced on the surface. On the other hand,

Thornton and Liu [30] simulated the particle dynamics using DEM, analysed the physical process of particle cluster breakage under impact load, and summarized four typical breakage modes: (I) Fracture, which includes obvious surface fractures or cracks, producing two or more relatively large fragments, and simultaneously, producing small fragments near the loading surface; (II) Shattering, in which relatively large fragments are broken down into smaller fragments via fracture; (III) Disintegration, which yields a relatively large fragment and several smaller fragments after breakage; (IV) Total disintegration, where entire particles undergo disintegration, leaving no large fragments postbreakage. The size distributions of fragments produced by shattering and total disintegration are similar; the difference lies in the system's kinetic energy after impact. During shattering, a large number of small fragments are ejected from the site of impact at relatively high velocities; while total disintegration involves the collapse of dissociated fragments into a pile. Based on the experimental phenomena observed in the numerical simulation, we adopted the three definitions of attrition, fracture, and shattering to describe particle breakage. A schematic diagram illustrating these modes is depicted in Figure 8. On this basis, the stages A, B, C, and D indicated in Figure 5 were used as divisions to analyse the process of evolution of particle breakage modes during the dynamic confined compression test on the sand specimen.

After the initial stage of elastic deformation, the particles began to break and the number of meso-cracks began to increase slowly at stage A. As depicted in Figure 9, the green particles in A-I approximated surface contact with the end face of the incident bar on the left and the orange particles on the right. After loading, the green particles exhibited obvious breakage, and the cracks primarily extended along the

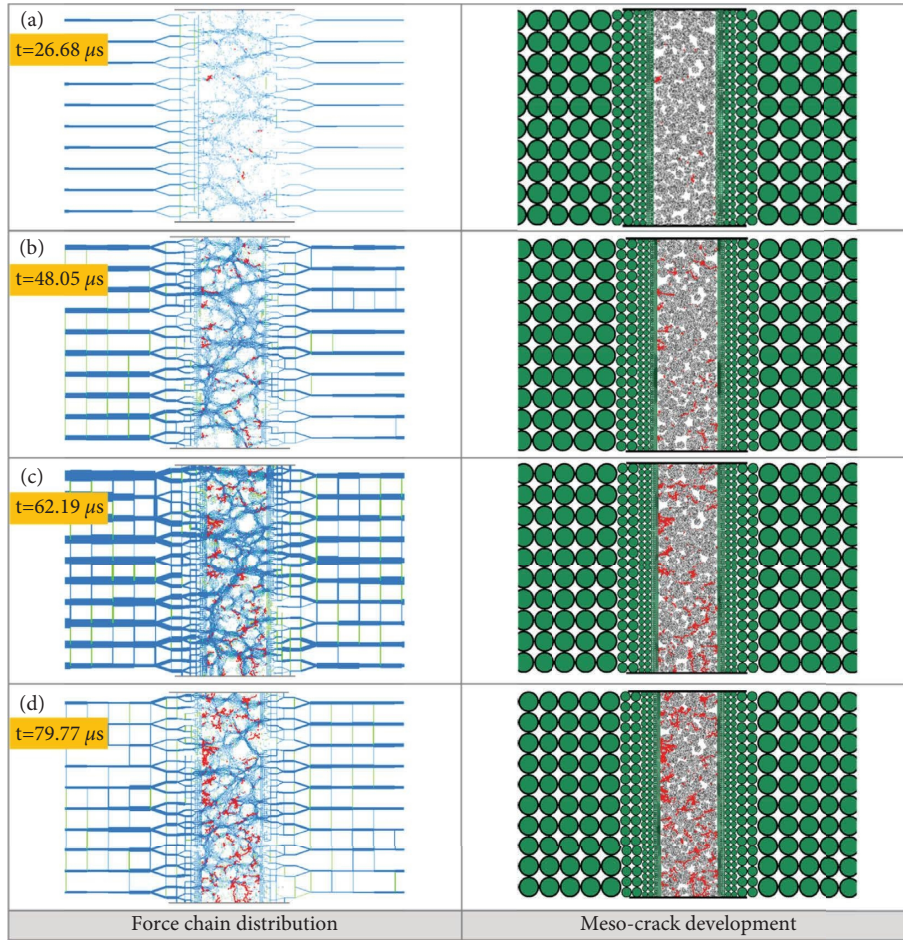


FIGURE 6: Force chain distribution and meso-crack development during the numerical compression test on the sand specimen. (a) $t=26.68 \mu s$, (b) $t=48.05 \mu s$, (c) $t=62.19 \mu s$, and (d) $t=79.77 \mu s$.

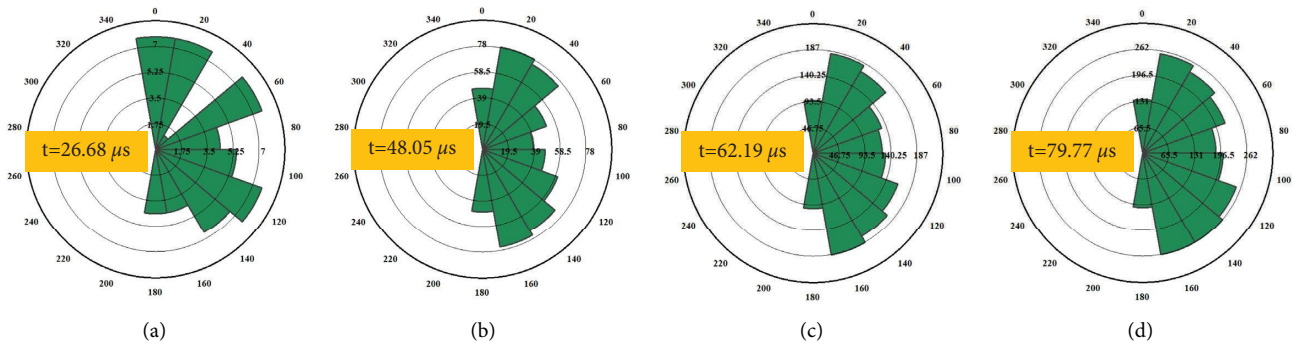


FIGURE 7: The process of evolution of crack anisotropy during the numerical compression test on the sand specimen. (a) $t=26.68 \mu s$, (b) $t=48.05 \mu s$, (c) $t=62.19 \mu s$, and (d) $t=79.77 \mu s$.

perpendicular to the contact surface and deflected up right under the influence of the internal pores. At this stage, the particles fractured and produced relatively large fragments in the lower part, while the upper part was broken into several smaller fragments. The blue and green particles in A-II occluded each other, which dislocated against each other under the action of force, generating cracks at the edges and corners. Thus, particle attrition occurred at the

edges and corners, and the initial occlusal structure was destroyed. In A-III, the contact between the grey and brown particles approximated point contact, where both particles exhibited attrition at the edges and corners, and the development of cracks exhibited an inward tendency. In A-IV, the yellow-green and dark green particles exhibited deeper occlusion than those in A-II. Thus, the yellow-green particle exhibited attrition at two corners and the dark-green particle

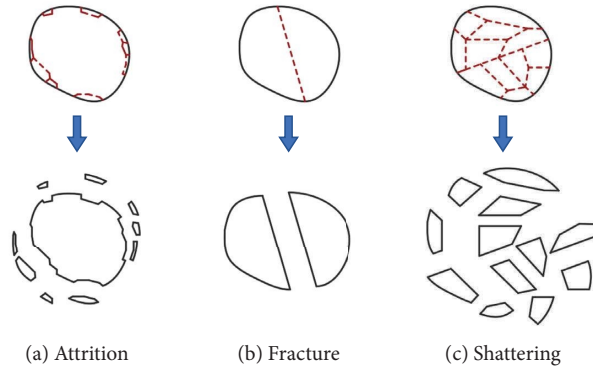


FIGURE 8: Schematic diagram depicting modes of particle breakage.

exhibited greater attrition, which produced small fragments on its right. Thus, in general, in stage A, except for a few shattering phenomena near the loading surface, particle breakage was dominated by the edge and corner attritions.

In stage (B), the load continued to be increased, and the breakage developed further, as depicted in Figure 10. In B-I, attrition was observed on the bottom right of the light-purple particle and crack initiation was observed at the contact position in the upper left of the particle. The crack in the yellow particle extended horizontally from the contact point on the left to that on the right, dividing the particle into upper and lower fragments, where the upper fragment slipped towards the external pores. In addition to the horizontal crack, a branch crack was detected on the upper right of the yellow particle, which extended through the inner pores to the contact point on the upper right and produced small fragments via shattering. The left part of the grey particle depicted in B-II exhibited local breakage at the contact point with the impact loading end. The crack penetrated and developed till the contact point between the grey particle and the dark green particle on the right. The green particle on the bottom left shattered near the loading end, and its fragments fell off and slipped. The cracks in the purple particle depicted in B-III were observed in multiple locations, exhibiting a shattered state. The compacted purple particle conducted the force chain to the blue particle on the right, where two cracks were initiated in its upper left and bottom left. In B-IV, the cracks penetrated the yellow-green and grey particles, causing the breakage of both. Simultaneous edge and corner attritions were also observed. In general, fracture was observed to be the predominant mode of breakage of particles in stage B, and the particles near the impact loading end were prone to local shattering.

The partial images corresponding to stages C and D were selected consistently with those in stage B to improve the analysis of the characteristics of particle breakage in different stages, as depicted in Figures 11 and 12. Compared to stage B, particle breakage was often accompanied by the weakening of the force chain in these cases, and the force transmission path was observed to shift from the breakage site to the relatively more complete particle fragments nearby. For example, the upper part of the light purple particle in C-I was fractured along the horizontal direction, which led to the weakening of the strong force chain in the original horizontal direction. Thus, the force was conducted through the lower residual fragment, and the

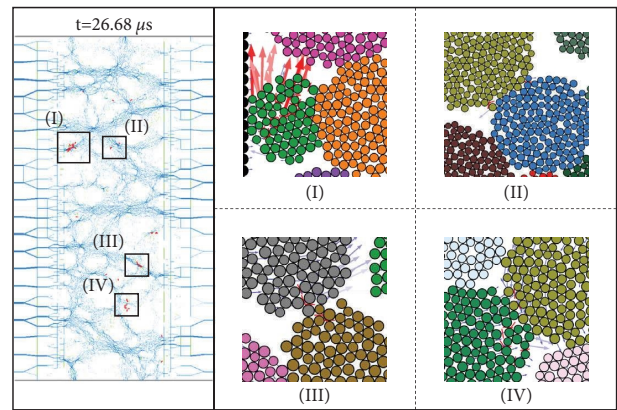


FIGURE 9: Breakage mode of the sand specimen during the numerical compression test (stage A).

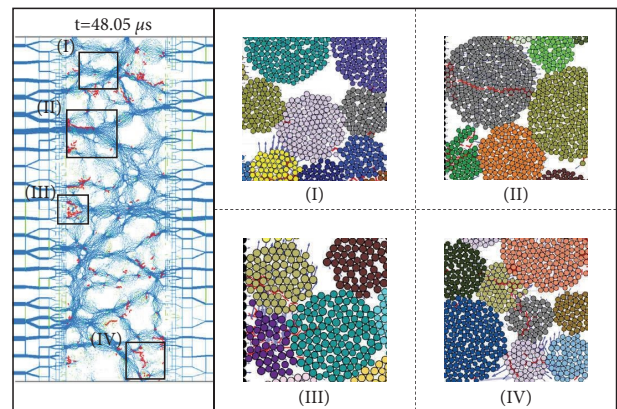


FIGURE 10: Breakage mode of the sand specimen during the numerical compression test (stage B).

strong force chain was transferred to the lower part. Via fracture, the lower part of the grey particle in C-II was shattered under further loading. The purple particle in C-III was further shattered, releasing the internal pores and resulting in local compaction. Following breakage, the upper fragment of the grey-green particle gained a certain degree of freedom and slipped towards the external pores. Finally, in C-IV, several through cracks were observed inside the particle. In summary, the degree

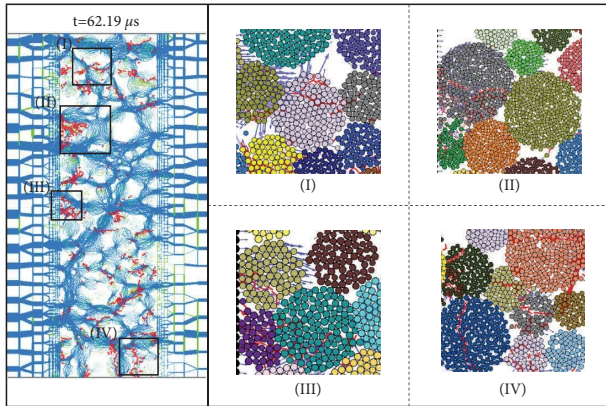


FIGURE 11: Breakage mode of the sand specimen during the numerical compression test (stage C).

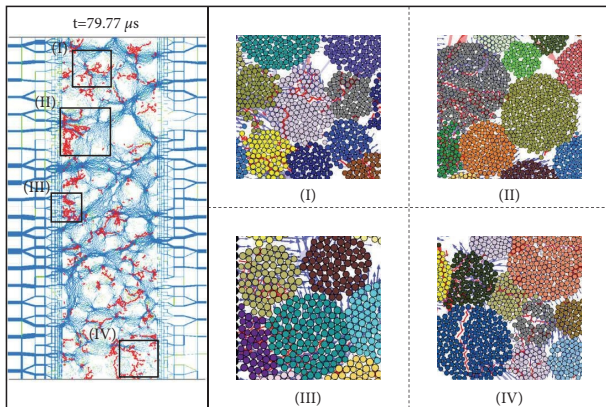


FIGURE 12: Breakage mode of the sand specimen during the numerical compression test (stage D).

of particle fracturing was observed to increase in stage C, the shattering of particles was observed in general, and the fragments slipped towards and filled the pores at an accelerated rate, which promoted the development of deformation.

After the breakage of a large number of particles, the overall force chain network was weakened in stage D, the overall density of the specimen became relatively high, and the fragments continued to slip and fall. Further, the dark green particles in D-II maintained relatively good integrity. This can be explained by the fact that this particle was wrapped and supported by surrounding particles, which produced an effect similar to confining pressure—reducing the uneven distribution of internal stress in the large particle and limiting its rotation and movement, thereby exerting a buffering effect on particle breakage [15, 31].

4. Conclusions

In this study, a DEM-based SHPB device with confinement and crushable coral sand particle aggregates were established. The force chain evolution, crack development, and variations in breakage modes during the particle breakage process were analysed. The main conclusions are as follows:

- (1) Following the generation of rigid particles with a certain gradation, they were replaced by basic unit aggregates with internal bonding bonds to simulate crushable sand particles. By considering the Weibull distribution and setting random numbers in the mesoscopic parameters, the particle strength results consistent with the laboratory test data were obtained.
- (2) With an increase in the load, the force chain evolved from a uniform distribution to one exhibiting a significant enhancement along the loading axis. The force chain weakened at sites of particle breakage and the force transmission path deviated towards the relatively more complete fragments nearby. During the unloading stage, the force chain network weakened as a whole.
- (3) Cracks were generated along the strong force chain and developed primarily along the loading axis. Particle breakage led to stress deflection, and the anisotropy of the cracks was weakened. Before yielding, particle breakage was not obvious in the sand specimen, and the deformation was caused by slipping particles and external pore compaction. After yielding, particle breakage became obvious, and the fragments slipped towards and filled the external pores, the void ratio decreased rapidly, and the compression deformation of the specimen was enhanced.
- (4) Under an impact load, particles near the loading surface were observed to be prone to shattering. Before yielding, particle breakage in the specimen was dominated by edge and corner attrition, and cracks appeared at the contact points of the particles, exhibiting a tendency to develop inward. After the specimen yielded, the crack extended into the particle perpendicular to the interparticle contact surface, and fracture was detected. Simultaneously, the crack was deflected by the presence of particle pores, thereby producing fragments of different sizes. Further particle breakage ensued via fracture and shattering, which was also observed. Further, when a particle was enveloped by multiple particles, an effect similar to confining pressure was generated during the loading process, buffering the breakage of the particle.

Data Availability

The data of this study are available from the corresponding author upon request.

Conflicts of Interest

The authors declare that they have no conflicts of interest.

Acknowledgments

This work was financed and fully supported by the National Natural Science Foundation of China (Grant no. 52222110), and Natural Science Foundation of Jiangsu Province of China (Grant No. BK20211230), which are greatly appreciated.

References

- [1] L. Ma, Z. Li, J. Liu, L. Duan, and J. Wu, "Mechanical properties of coral concrete subjected to uniaxial dynamic compression," *Construction and Building Materials*, vol. 199, no. 28, pp. 244–255, 2019.
- [2] H. Ma, C. Yue, and H. Yu, "Experimental study and numerical simulation of impact compression mechanical properties of high strength coral aggregate seawater concrete," *International Journal of Impact Engineering*, vol. 137, no. 8, pp. 103466.1–103466.13, 2020.
- [3] L. Ma, Z. Li, M. Wang, H. Wei, and P. Fan, "Effects of size and loading rate on the mechanical properties of single coral particles," *Powder Technology*, vol. 382, pp. 961–971, 2019.
- [4] W. R. Bryant, A. P. Deflache, and P. K. Trabant, *Consolidation of marine Clays and Carbonates*, Deep-sea sediments. Springer, Boston, MA, USA, 1974.
- [5] M. R. Coop, "The mechanics of uncemented carbonate sands," *Géotechnique*, vol. 40, no. 4, pp. 607–626, 1990.
- [6] C. Wang, X. Ding, and Y. Xiao, "Effects of relative densities on particle breaking behaviour of non-uniform grading coral sand," *Powder Technology*, vol. 382, pp. 524–531, 2021.
- [7] M. Datta, S. K. Gulhati, and G. V. Rao, "Crushing of calcareous sands during shear," in *Proceedings of the Offshore Technology Conference*, Offshore Technology Conference, Houston, Asia, October 1979.
- [8] L. Luzzani and M. Coop, "On the relationship between particle breakage and the critical state of sands," *Soils and Foundations*, vol. 42, no. 2, pp. 71–82, 2002.
- [9] G. Wang, Z. Wang, Q. Ye, and J. Zha, "Particle breakage evolution of coral sand using triaxial compression tests," *Journal of Rock Mechanics and Geotechnical Engineering*, vol. 13, no. 2, pp. 321–334, 2021.
- [10] L. Ma, J. Wu, M. Wang, L. Dong, and H. Wei, "Dynamic compressive properties of dry and saturated coral rocks at high strain rates," *Engineering Geology*, vol. 272, Article ID 105615, 2020.
- [11] H. Zhang, L. Ma, Z. Luo, and N. Zhang, "Wave attenuation and dispersion in a 6 mm diameter viscoelastic Split Hopkinson pressure bar and its correction method," *Shock and Vibration*, vol. 2020, no. 821, Article ID 8888445, 10 pages, 2020.
- [12] X. Yu, L. Chen, Q. Fang, J. Zhang, D. Guo, and X. Hou, "Determination of attenuation effects of coral sand on the propagation of impact-induced stress wave," *International Journal of Impact Engineering*, vol. 125, pp. 63–82, 2019.
- [13] G. R. McDowell and O. Harireche, "Discrete element modelling of soil particle fracture," *Géotechnique*, vol. 52, no. 2, pp. 131–135, 2002.
- [14] L. Elghezal, M. Jamei, and I. O. Georgopoulos, "DEM simulations of stiff and soft materials with crushable particles: an application of expanded perlite as a soft granular material," *Granular Matter*, vol. 15, no. 5, pp. 685–704, 2013.
- [15] D. M. Kuang, Z. I. Long, R. Q. Guo, and P. Yu, "Numerical investigation of the cushion and size effects during single-particle crushing via DEM," *Acta Mechanica Sinica*, vol. 33, no. 6, pp. 851–863, 2020.
- [16] B. Zhao, C. Chow, and J. Wang, "An investigation of single particle crushing tests on irregular-shaped quartz sand with DEM," in *Proceedings of the International Conference on Discrete Element Methods*, Springer, Singapore, June 2017.
- [17] S. Liu and T. Lok, *Discrete Element Simulation of Particle Crushing in 1-D Compression*, Springer, Singapore, 2018.
- [18] T. Zhang, C. Zhang, J. Zou, B. Wang, F. Song, and W. Yang, "DEM exploration of the effect of particle shape on particle breakage in granular assemblies," *Computers and Geotechnics*, vol. 122, Article ID 103542, 2020.
- [19] J. Huang, S. Xu, and S. Hu, "Effects of grain size and gradation on the dynamic responses of quartz sands," *International Journal of Impact Engineering*, vol. 59, pp. 1–10, 2013.
- [20] H. Yang, W. J. Xu, Q. C. Sun, and Y. Feng, "Study on the meso-structure development in direct shear tests of a granular material," *Powder Technology*, vol. 314, pp. 129–139, 2017.
- [21] Y. Luo, G. Wang, X. Li et al., "Analysis of energy dissipation and crack evolution law of sandstone under impact load," *International Journal of Rock Mechanics and Mining Sciences*, vol. 132, Article ID 104359, 2020.
- [22] X. F. Li, X. Li, H. B. Li, Q. Zhang, and J. Zhao, "Dynamic tensile behaviours of heterogeneous rocks: the grain scale fracturing characteristics on strength and fragmentation," *International Journal of Impact Engineering*, vol. 118, pp. 98–118, 2018.
- [23] M. Ghadiri, R. Moreno-Atanasio, and A. Hassanpour, "Analysis of agglomerate breakage," *Handbook of Powder Technology*, vol. 12, pp. 837–872, 2007.
- [24] G. Cai, L. Xia, and J. Guo, "Microparameter analysis of particle breakage model based on impact experiment [J]," *China Powder Science and Technology*, vol. 22, no. 120, pp. 46–50, 2016.
- [25] Y. Nakata, M. Hyodo, A. F. L. Hyde, Y. Kato, and H. Murata, "Microscopic particle crushing of sand subjected to high pressure one-dimensional compression," *Soils and Foundations*, vol. 41, no. 1, pp. 69–82, 2001.
- [26] D. Shi, J. Zhou, and M. Jia, "Numerical simulations of particle breakage property of sand under high pressure 1D compression condition by use of particle flow code," *Chinese Journal of Geotechnical Engineering*, vol. 5, pp. 736–742, 2007.
- [27] Q. Sun, H. Xin, and J. Liu, "Skeleton and force chain network in static granular material," *Rock and Soil Mechanics*, vol. 30, no. 1, pp. 83–87, 2009.
- [28] P. Feng, M. Wei, F. Dai, R. Tang, H. Qiu, and J. Gong, "DEM investigation on the mechanical behaviors of flawed specimens subjected to coupled static-dynamic loads," *Soil Dynamics and Earthquake Engineering*, vol. 135, Article ID 106220, 2020.
- [29] É Guyon and J. P. Troadec, *Du sac de billes au tas de sable*, Odile Jacob, Paris, France, 1994.
- [30] C. Thornton and L. Liu, "How do agglomerates break," *Powder Technology*, vol. 144, pp. 110–116, 2004.
- [31] J. Fonseca, P. Bésuelle, and G. Viggiani, "Micromechanisms of inelastic deformation in sandstones: an insight using x-ray micro-tomography," *Géotechnique Letters*, vol. 3, no. 2, pp. 78–83, 2013.